Alloy Nanoclusters Artificial Photosystems Steering Photoredox Organic Transformation

Bing-Xiong Zheng [a], Jiao-Nan Yuan[a], Peng Su [a], Xian Yan [a], Qing Chen [a], Meng Yuan [a], Fang-Xing Xiao[a, b]*

a. College of Materials Science and Engineering, Fuzhou University, New Campus, Minhou, Fujian Province, 350108, China.

b. State Key Laboratory of Structural Chemistry, Fujian Institute of Research on the Structure of Matter, Chinese Academy of Sciences, Fuzhou, Fujian 350002, PR China.

E-mail: fxxiao@fzu.edu.cn

Table of Contents

Page NO.

Experimental section

1. Materials

Deionized water (DI H_2O, Millipore, 18.2 MΩ cm resistivity), sodium diethyldithiocarbamate trihydrate ($C_5H_{10}NNaS_2 \cdot 3H_2O$), cadmium chloride ($CdCl_2 \cdot 2.5H_2O$), ethylenediamine ($C_2H_8N_2$), 2-mercaptoethylamine (MEA), tetrachloroauric (III) acid ($HAuCl_4 \cdot 3H_2O$, 99.99%), silver nitrate ($AgNO_3$), L-glutathione (GSH), 4-nitroaniline (4-NA), 3-nitroaniline (3-NA), 2-nitroaniline (2-NA), 4-nitrophenol (4-NP), 3-nitrophenol (3-NP), 2-nitrophenol (2-NP), 1-bromo-4-nitrobenzene, 1-chloro-4-nitrobenzene, 4-nitroanisole, 4-nitrotoluene (4-NT), nitrobenzene (NB), o-nitroacetophenone were obtained from Sinopharm Chemical Reagent Co, Ltd. (Shanghai, China). benzyl alcohol (BA), *p*-methylbenzyl alcohol, *p*-methoxybenzyl alcohol (MOBA), *p*-fluorobenzyl alcohol, *p*-chlorobenzyl alcohol, *p*-nitrobenzyl alcohol, and 3-methyl-2-buten-1-ol potassium peroxydisulfate ($K_2S_2O_8$), benzoquinone (BQ), ammonium oxalate (AO), *tert*-butanol (*t*-BuOH) was obtained from Sigma-Aldrich. All materials were used as received without further purification.

2 Preparation of photoelectrodes

The working electrodes were prepared on fluorine-dope tin oxide (FTO) glass that was cleaned by sonication in ethanol for 30 min and dried at 353 K. The boundary of FTO glass was protected using scotch tape. The 5 mg sample was completely dispersed in 0.5 mL of ethyl alcohol absolute by sonication to get slurry which uniformly was spread onto the pretreated FTO glass. After drying in the air, the working electrode was further dried at 353K for 2 h to improve adhesion. Then the Scotch tape was unstuck and the exposed area of the working electrode was 1 cm2. Besides, Na_2SO_4 (0.5 M, pH=6.69) aqueous solution was used as the electrolyte

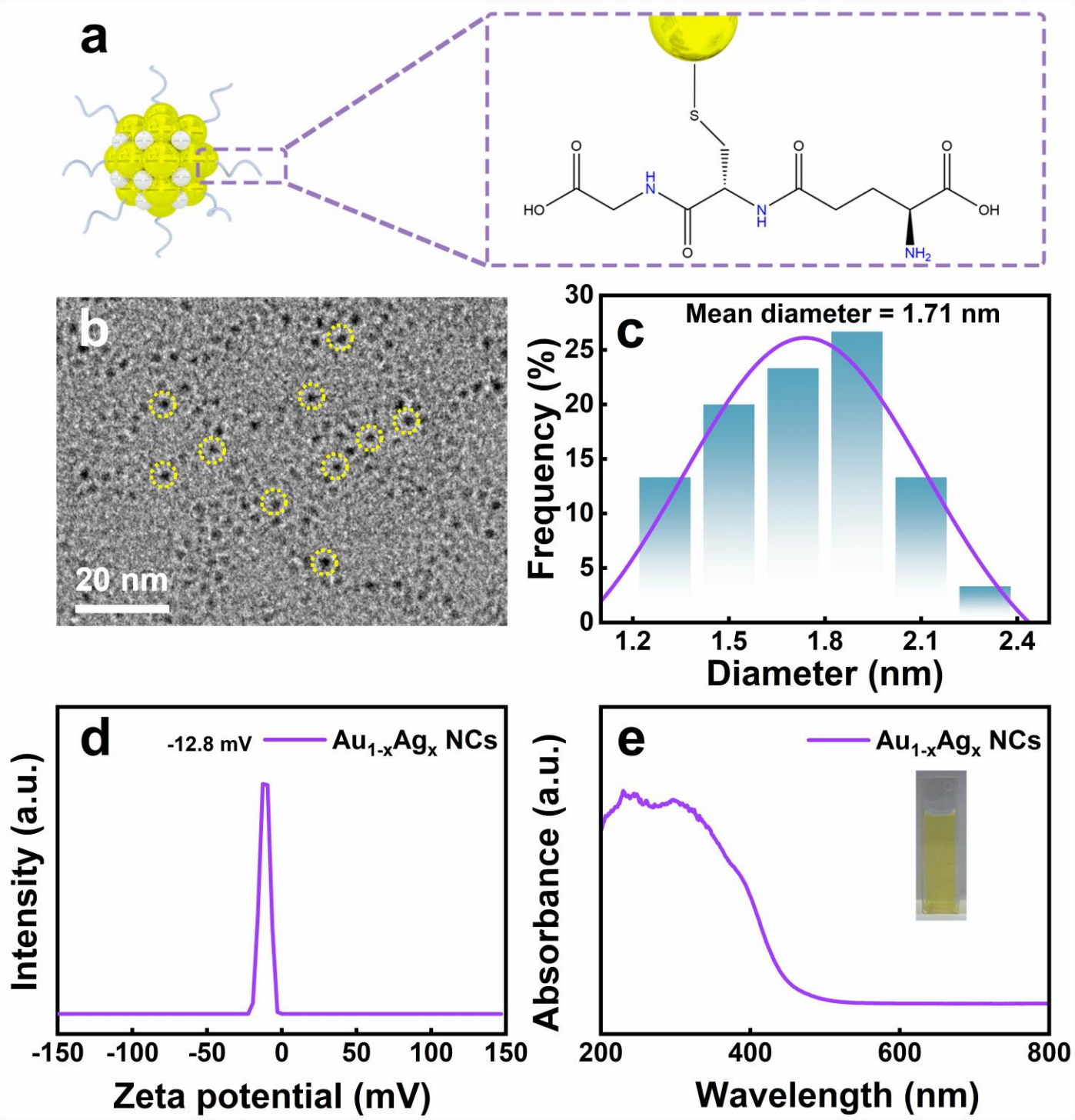

Figure S1. (a)Schematic model illustrating the molecule structure of $Au_{1-x}Ag_x$ NCs and surface ligand (GSH), (b) TEM image of $Au_{1-x}Ag_x$ NCs, (c) size distribution histogram, (d) zeta potential of $Au_{1-x}Ag_x$ NCs, (e) UV-vis absorption spectrum of $Au_{1-x}Ag_x$ NCs with photograph in the inset.

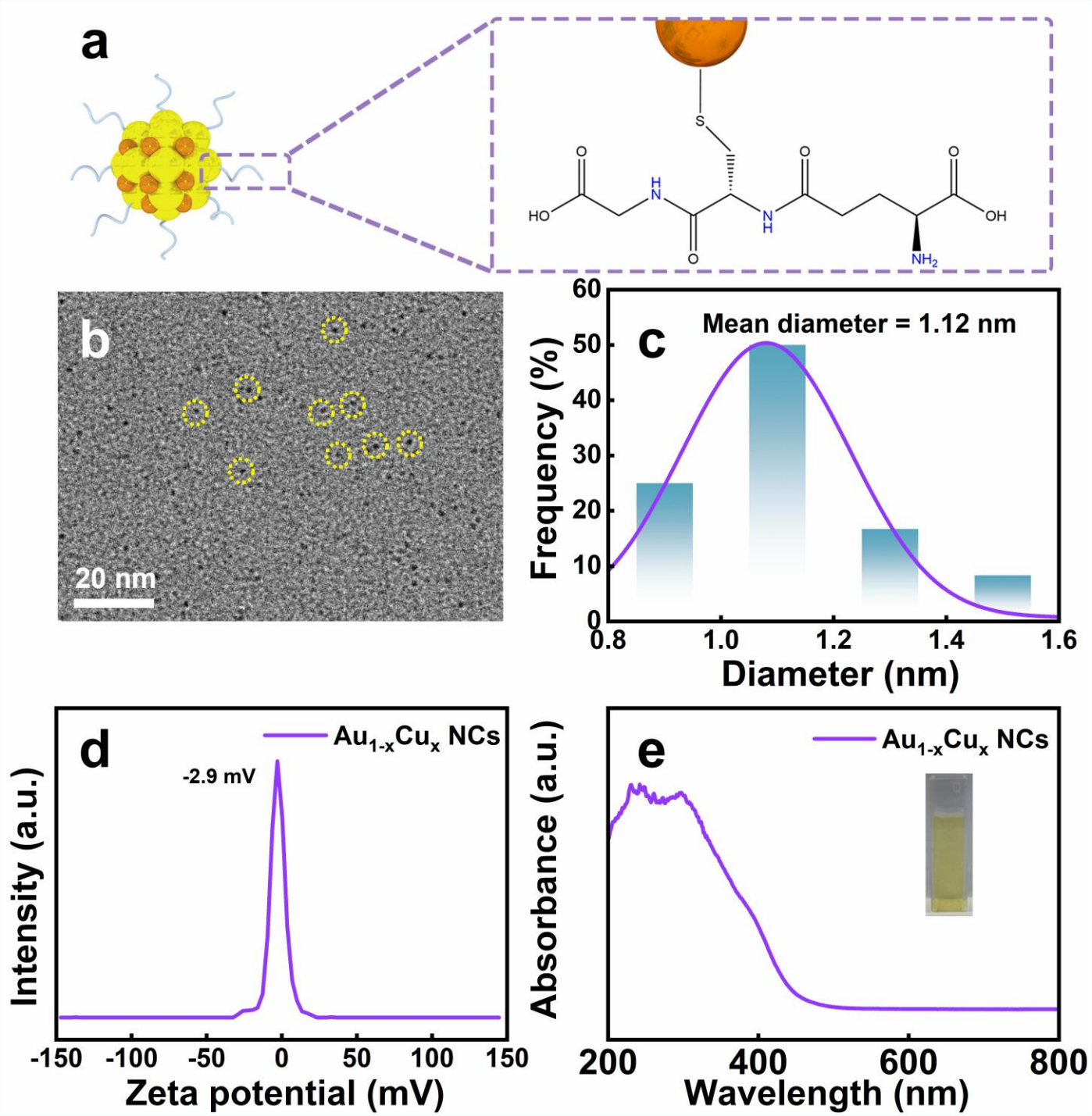

Figure S2. (a)Schematic model illustrating the molecule structure of $Au_{1-x}Cu_x$ NCs and surface ligand (GSH), (b) TEM image of $Au_{1-x}Cu_x$ NCs, (c) size distribution histogram, (d) zeta potential of $Au_{1-x}Cu_x$ NCs, (e) UV-vis absorption spectrum of $Au_{1-x}Cu_x$ NCs with photograph in the inset.

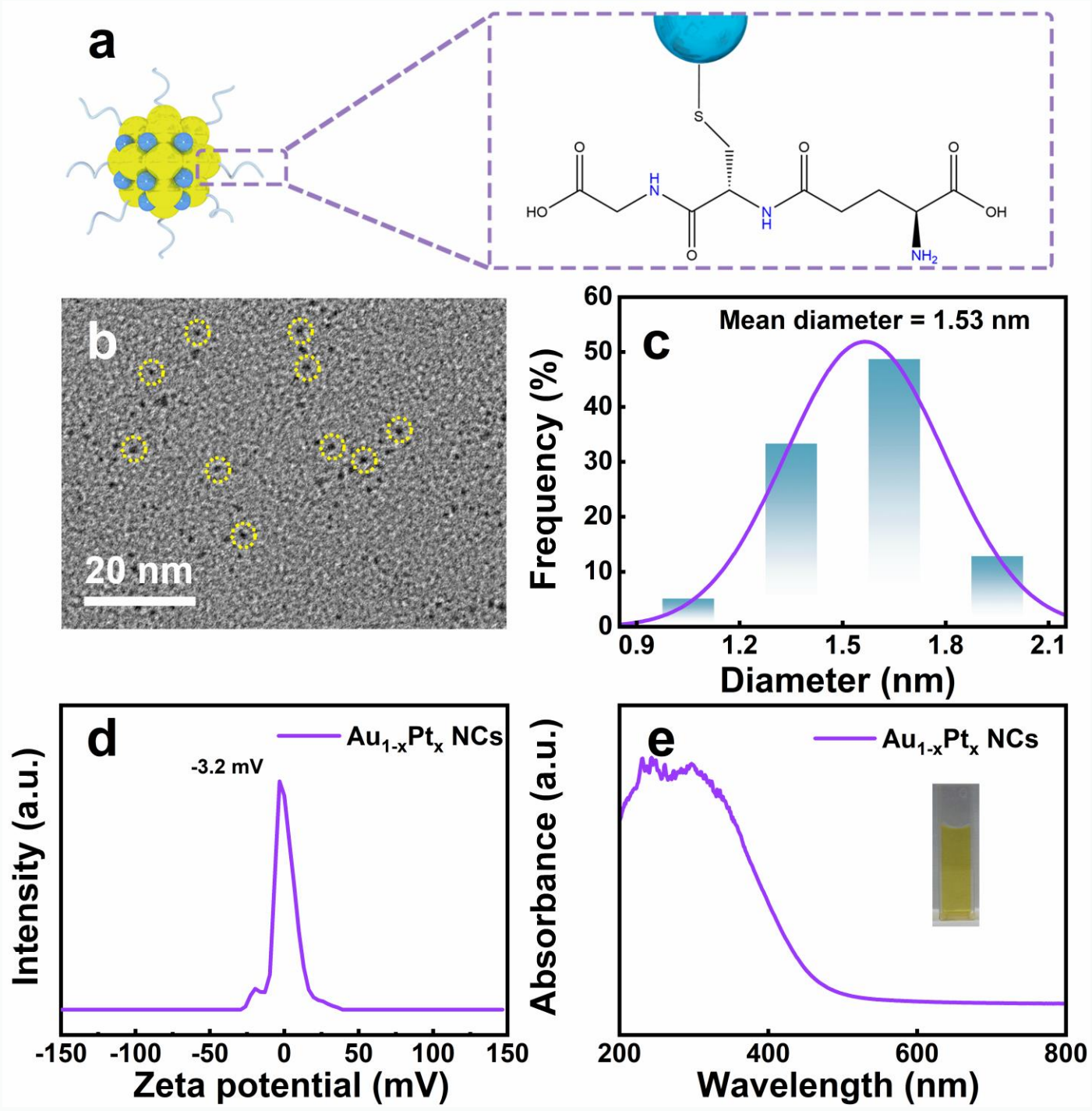

Figure S3. (a)Schematic model illustrating the molecule structure of $Au_{1-x}Pt_x$ NCs and surface ligand (GSH), (b) TEM image of $Au_{1-x}Pt_x$ NCs, (c) size distribution histogram, (d) zeta potential of $Au_{1-x}Pt_x$ NCs, (e) UV-vis absorption spectrum of $Au_{1-x}Pt_x$ NCs with photograph in the inset.

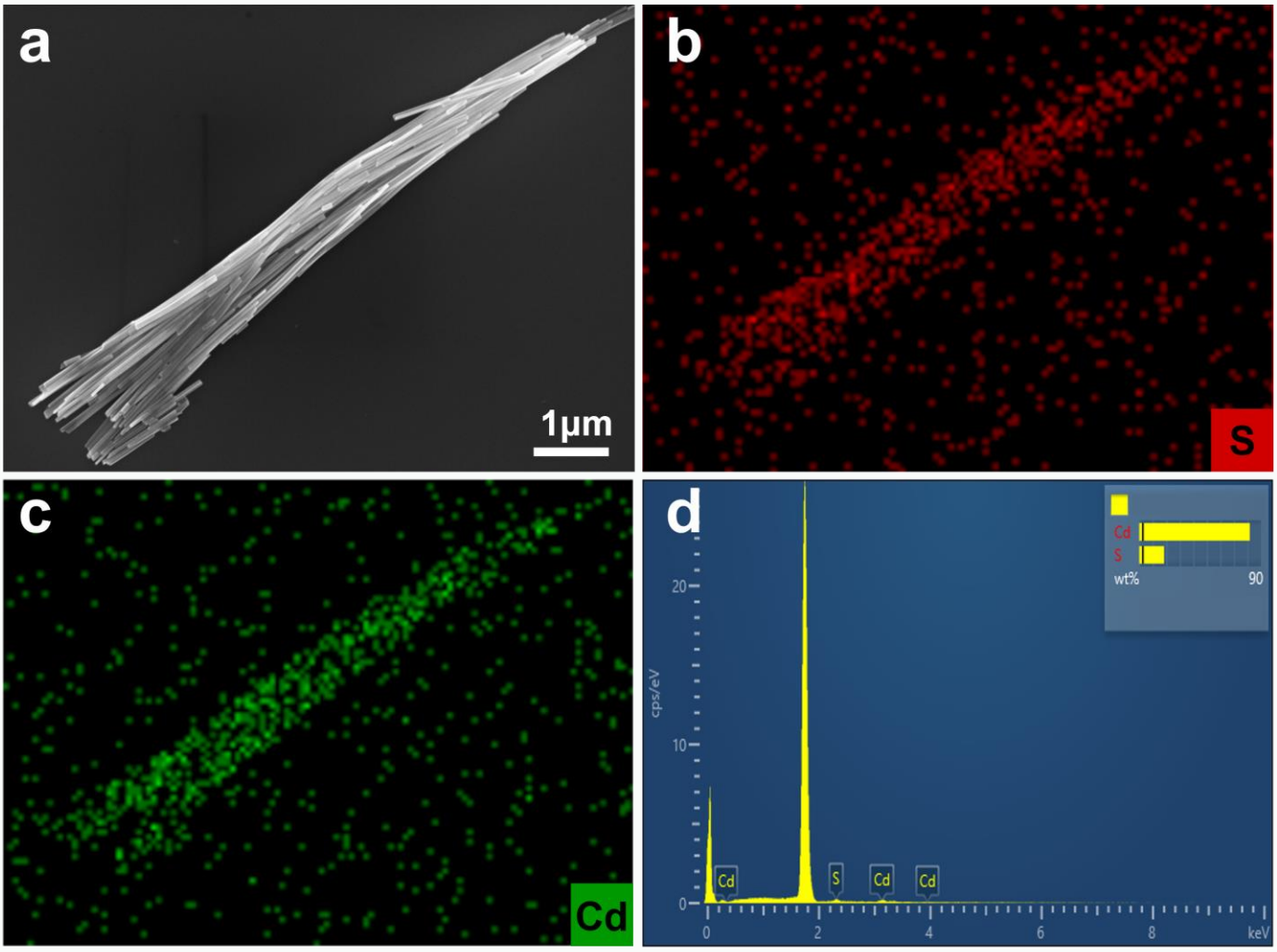

Figure S4. (a) SEM images of CdS NWs and (b-c) elemental mapping results of CdS NWs along with (d) EDS result.

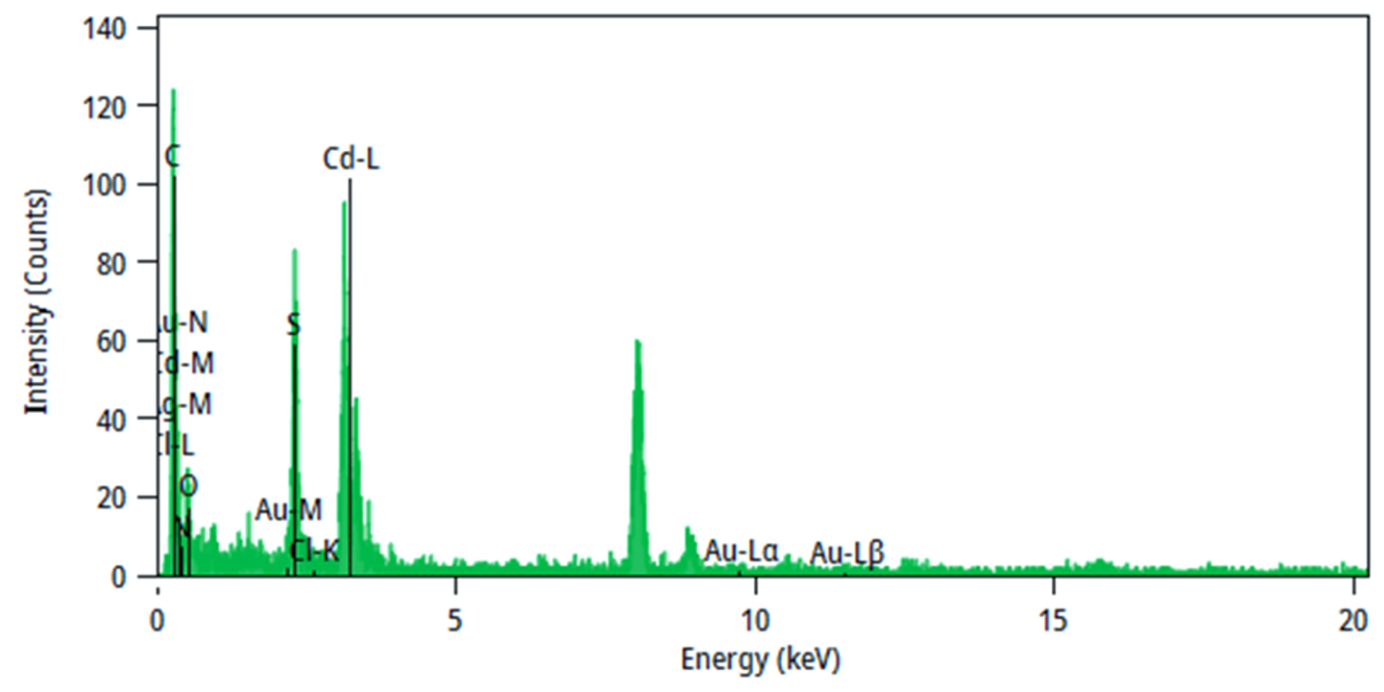

Figure S5. EDS result of $Au_{1-x}Ag_x$/CdS NWs

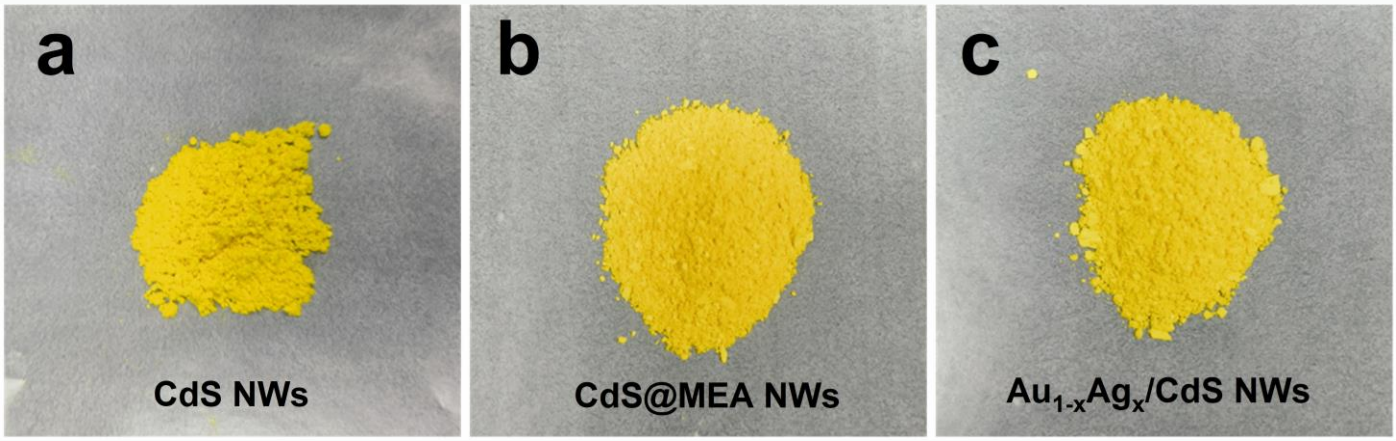

Figure S6. Sample colors of (a) CdS NWs, (b) CdS@MEA NWs and (c) $Au_{1-x}Ag_x$/CdS NWs heterostructure.

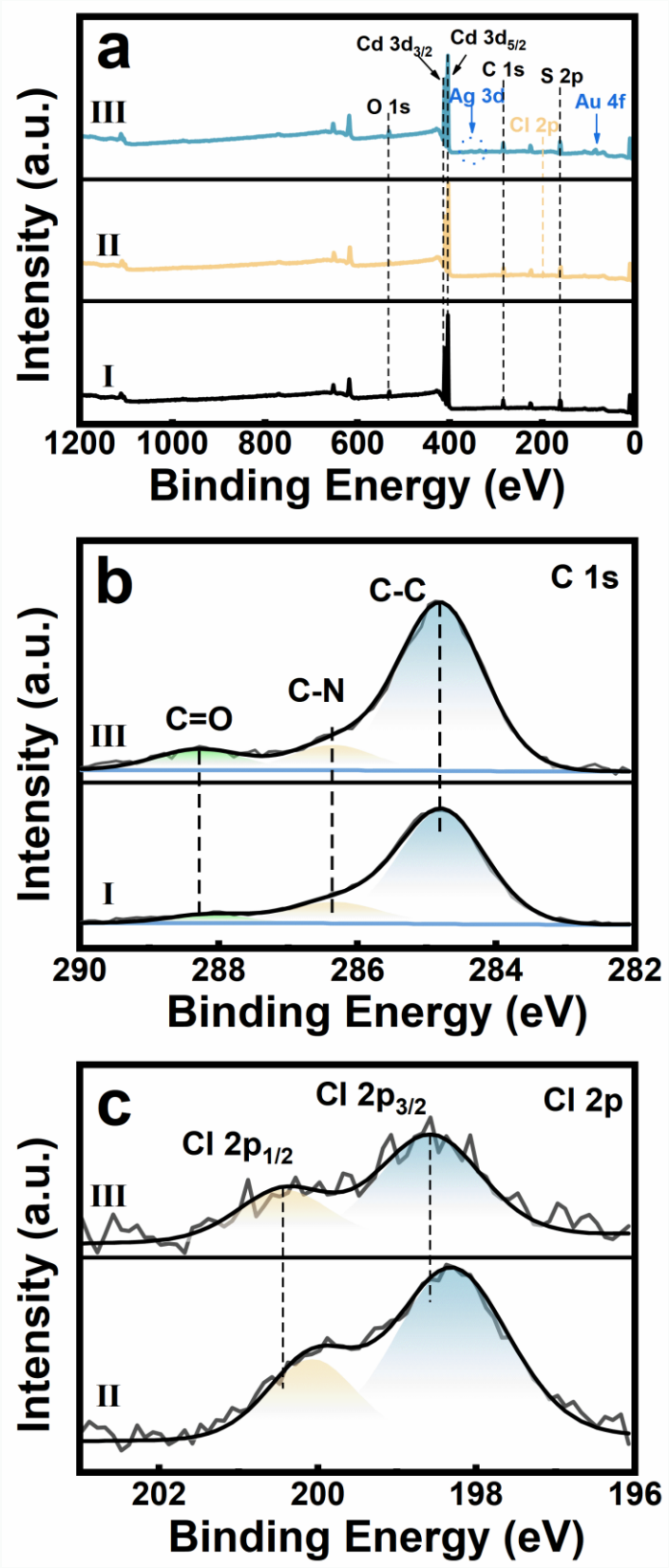

Figure S7. (a) Survey spectra and high-resolution (b) C 1s and (c) Cl 2p spectra of (I) CdS NWs, (II) CdS@MEA NWs and (III) $Au_{1-x}Ag_x$/CdS NWs heterostructure.

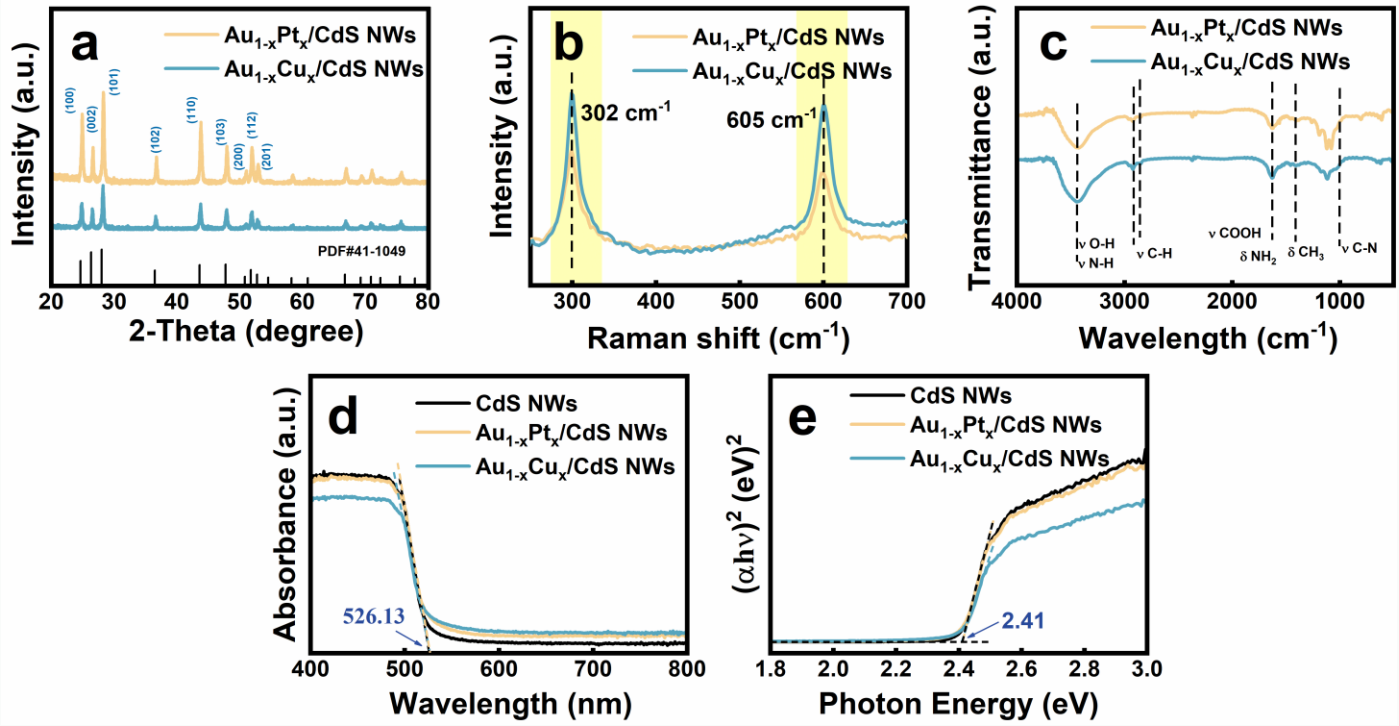

Figure S8. (a) XRD results, (b) Raman, (c) FTIR, (d) DRS results of pristine CdS, $Au_{1-x}Pt_x$/CdS NWs and $Au_{1-x}Cu_x$/CdS NWs heterostructure with (e) bandgap determination plots.

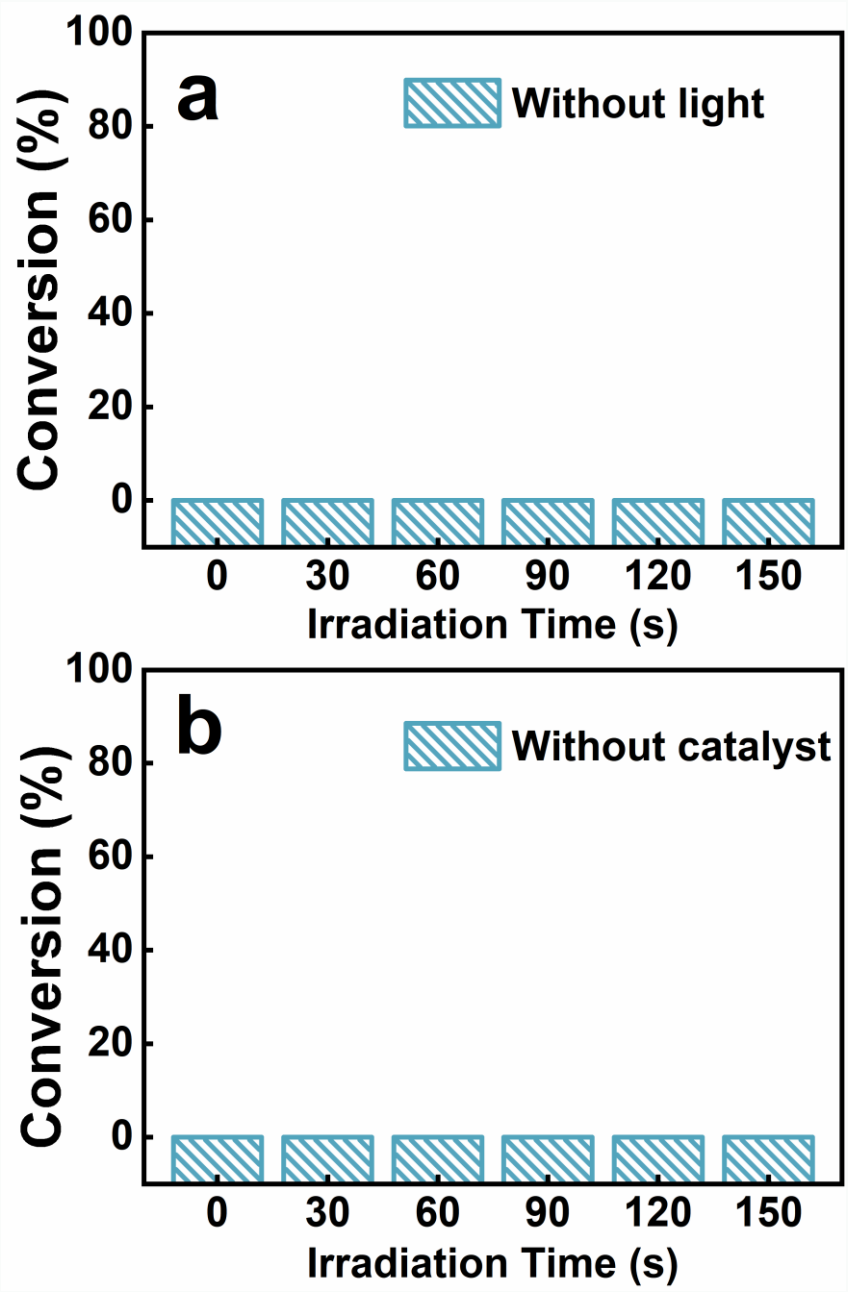

Figure S9. Blank experiments for photocatalytic reduction of 4-NA (a) without light and (b) catalyst.

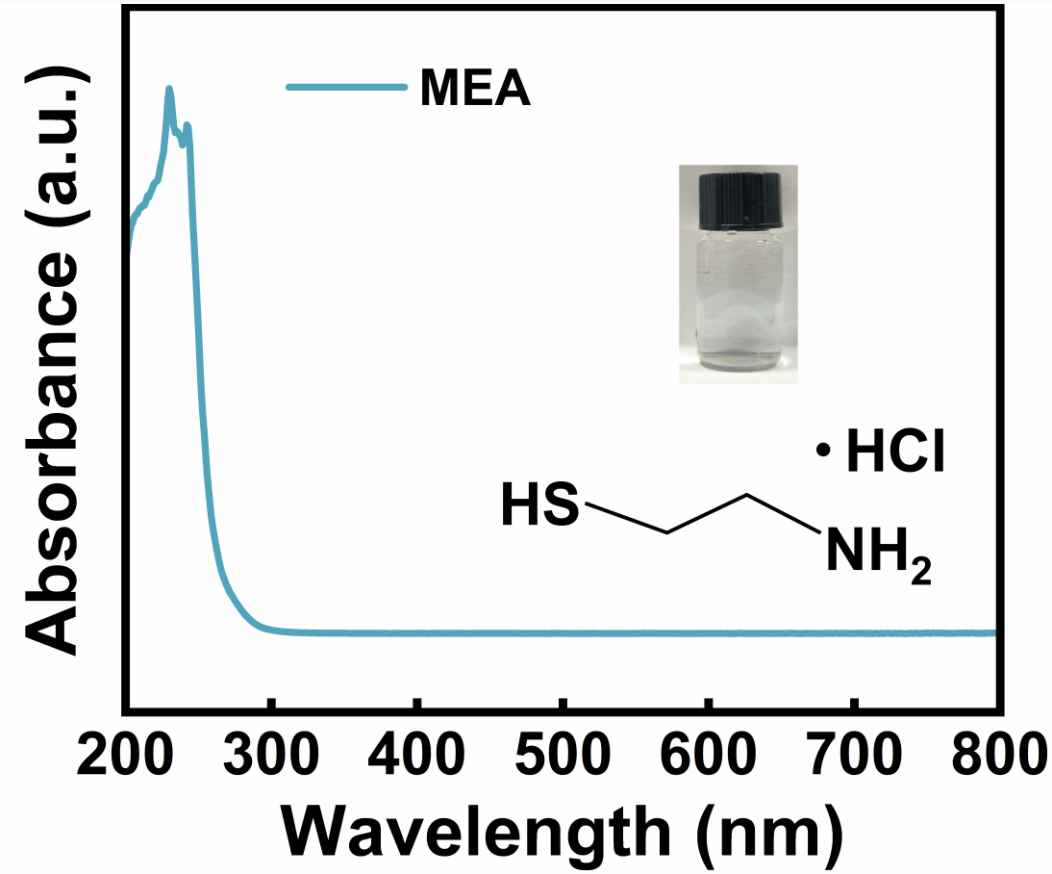

Figure S10. UV-vis absorption spectrum of MEA aqueous solution with photograph and molecular structure in the inset.

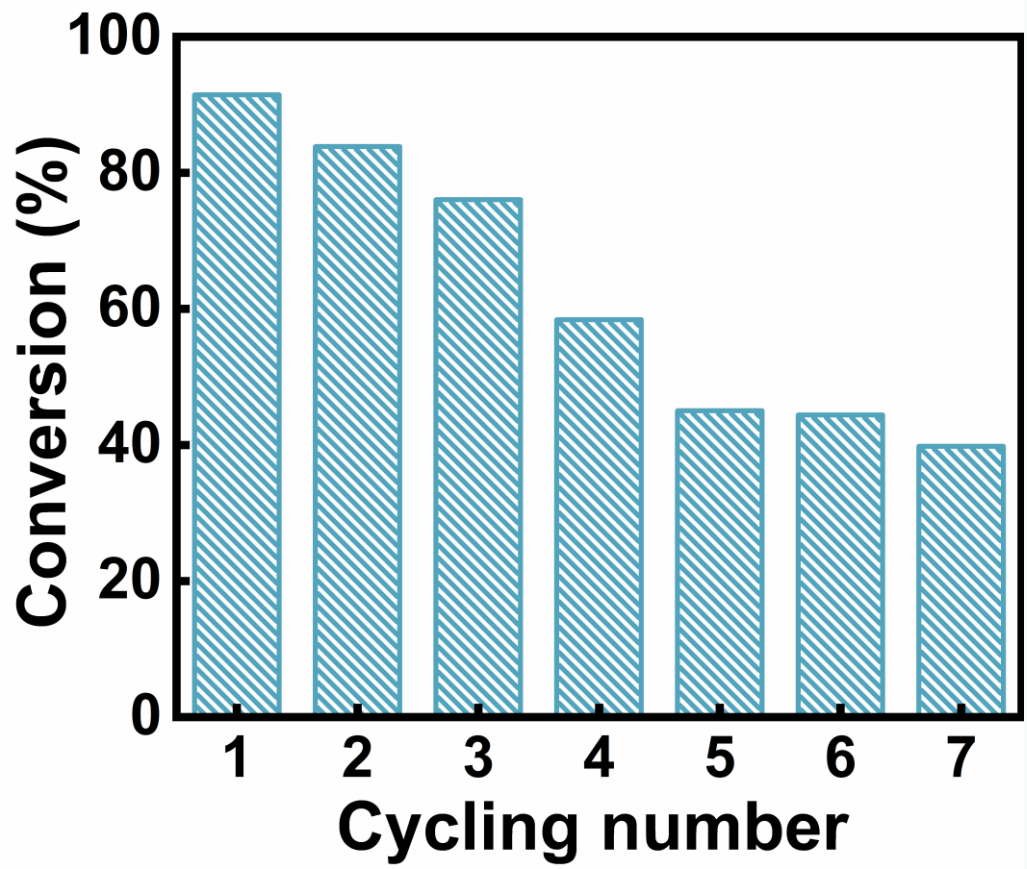

Figure S11. Cyclic reactions of $Au_{1-x}Ag_x$ /CdS NWs heterostructure toward photoreduction of 4-NA.

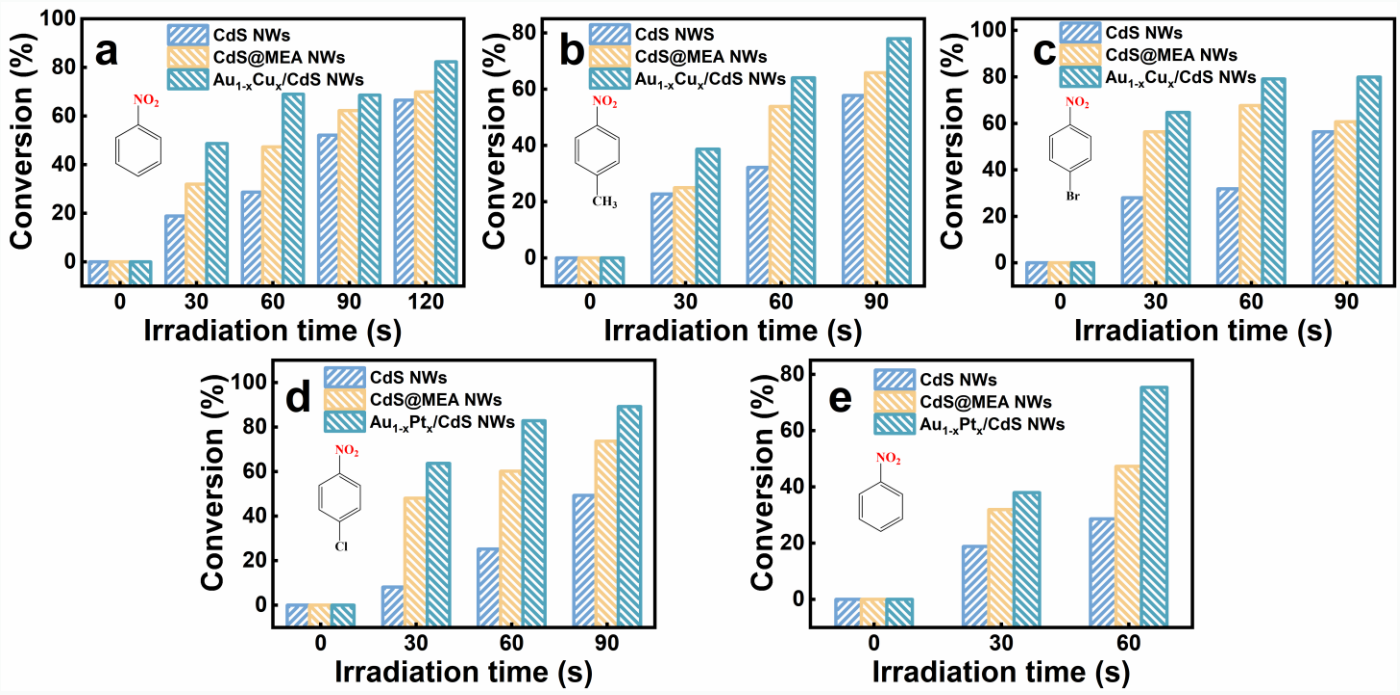

Figure S12. Photoactivities of pristine CdS NWs, CdS@MEA NWs, and $Au_{1-x}Cu_x$/CdS NWs heterostructure towards photoreduction of (a) NB, (b) 4-NT, and (c) 1-bromo-4-nitrobenzene, under visible light irradiation (λ>420 nm) with adding hole scavenger and nitrogen bubbling at ambient conditions. Photoactivities of pristine CdS NWs, CdS@MEA NWs, and $Au_{1-x}Pt_x$/CdS NWs heterostructure towards photo reduction of (d) 1-chloro-4-nitrobenzene, (e) NB under visible light irradiation (λ>420 nm).

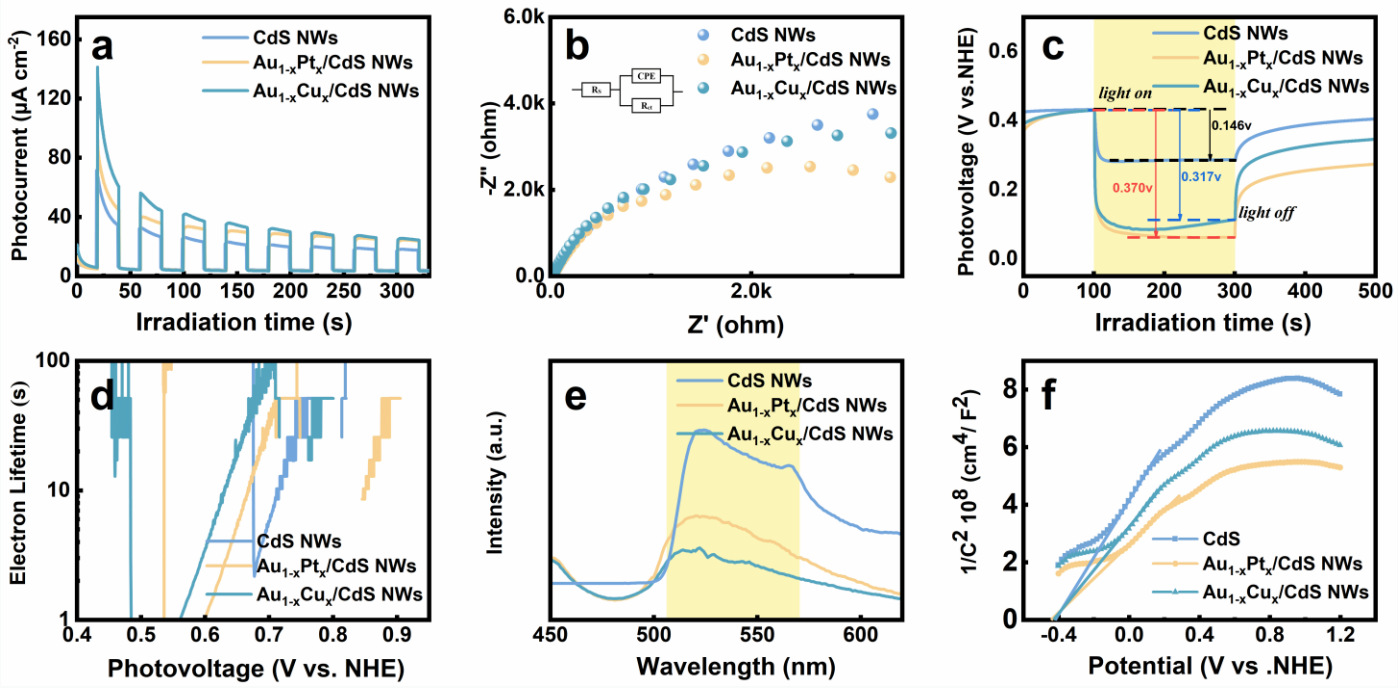

Figure S13. (a) On−off transient photocurrents, (b) EIS results, (c) open-circuit potential decays and (d) electron lifetime (τ_n), and (e) PL spectra of pristine CdS NWs, $Au_{1-x}Pt_x$/CdS NWs and $Au_{1-x}Cu_x$/CdS NWs heterostructure as well as (f) Mott-Schottky plots.

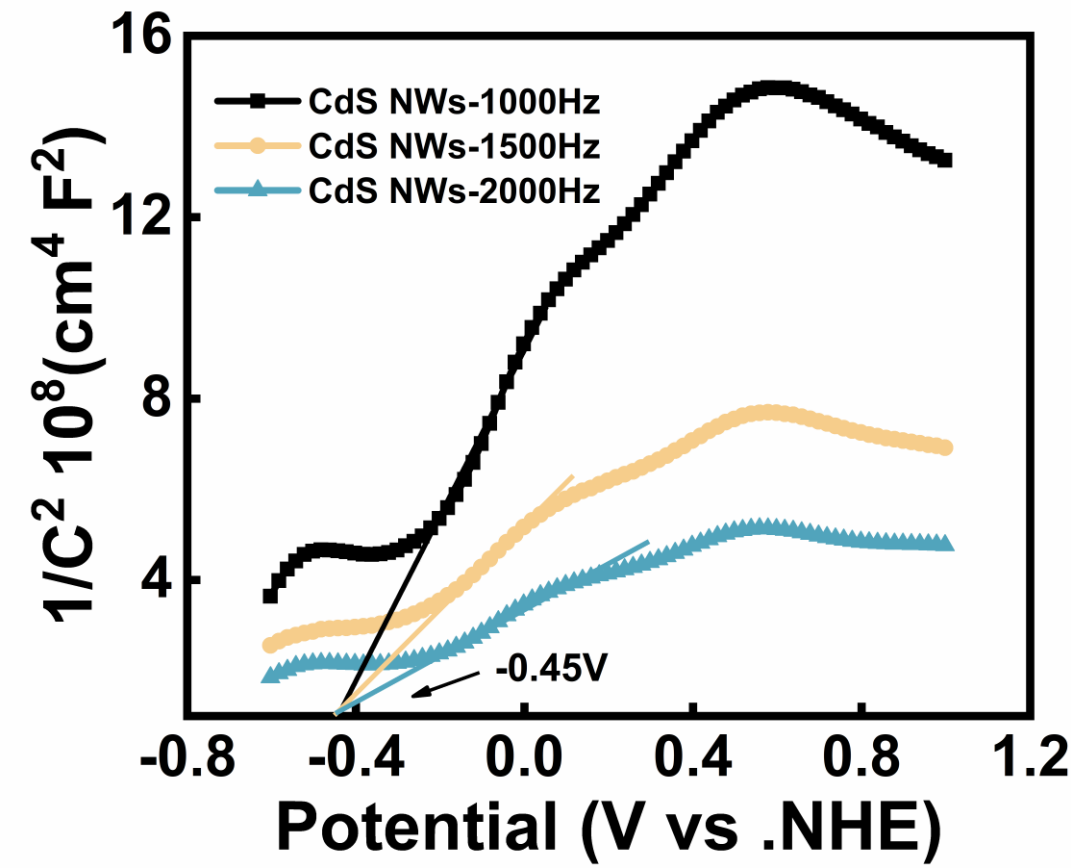

Figure S14. Mott-Schottky plots of CdS NWs probed under different frequencies.

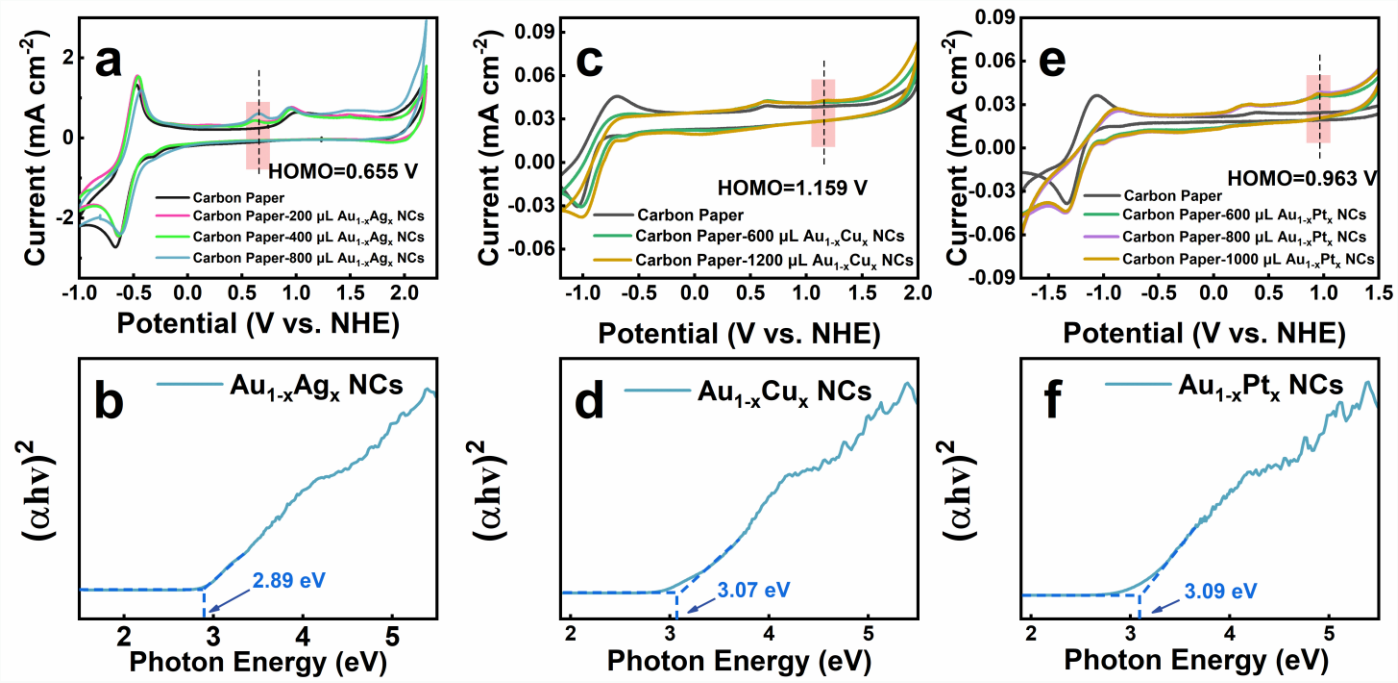

Figure S15. CV curves of (a) $Au_{1-x}Ag_x$ NCs, (c) $Au_{1-x}Cu_x$ NCs and (e) $Au_{1-x}Pt_x$ NCs. (electrolyte: degassed acetonitrile containing 0.1 mol L^{-1} TEAP); Transformed plots based on the Kubelka–Munk function vs. energy of light for (b) $Au_{1-x}Ag_x$ NCs, (d) $Au_{1-x}Cu_x$ NCs and (f) $Au_{1-x}Pt_x$ NCs.

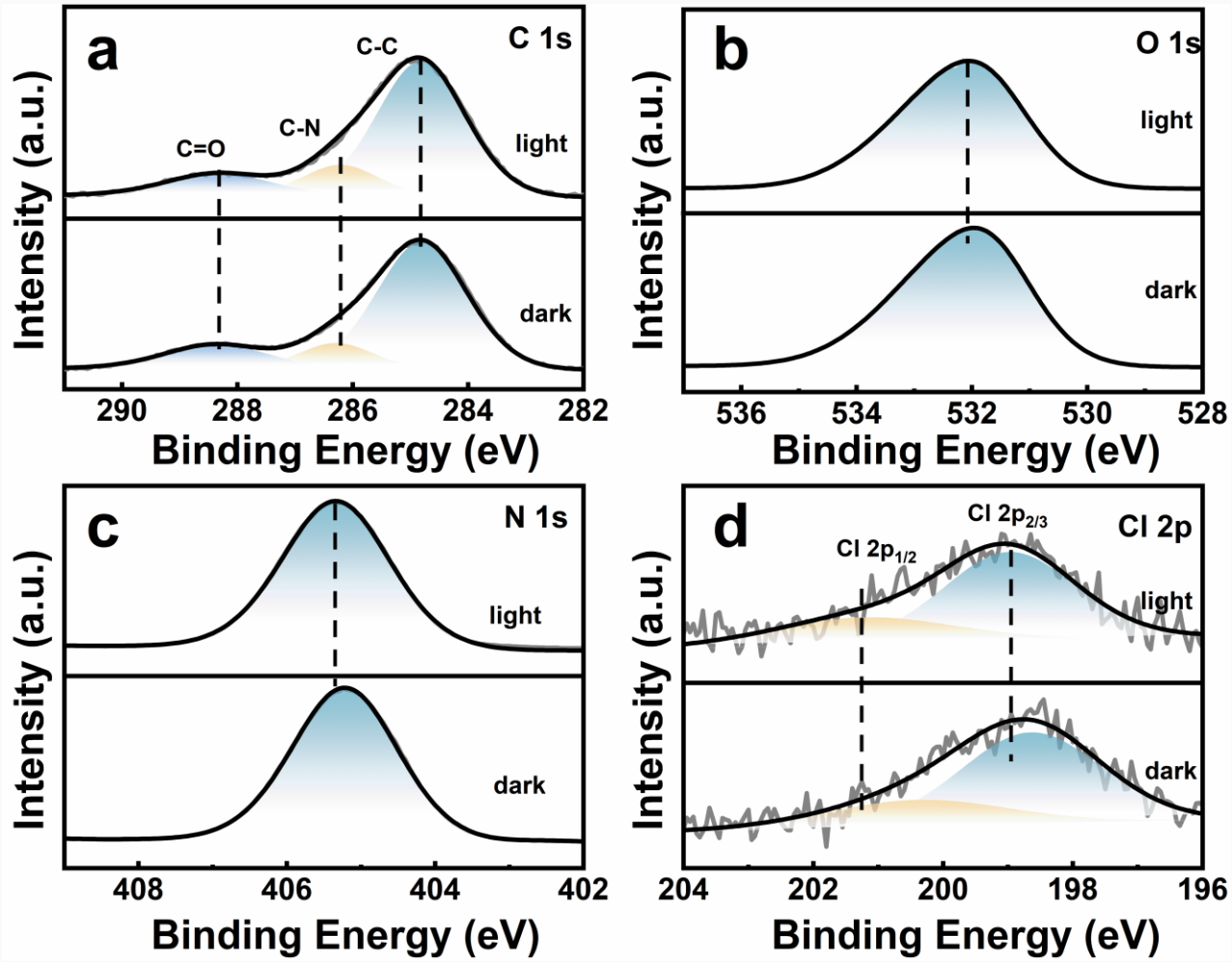

Figure S16. In-situ high-resolution XPS spectra of (a) C 1s, (b) O 1s (c) N 1s (d) Cl 2p for $Au_{1-x}Ag_x$/CdS NWs heterostructure.

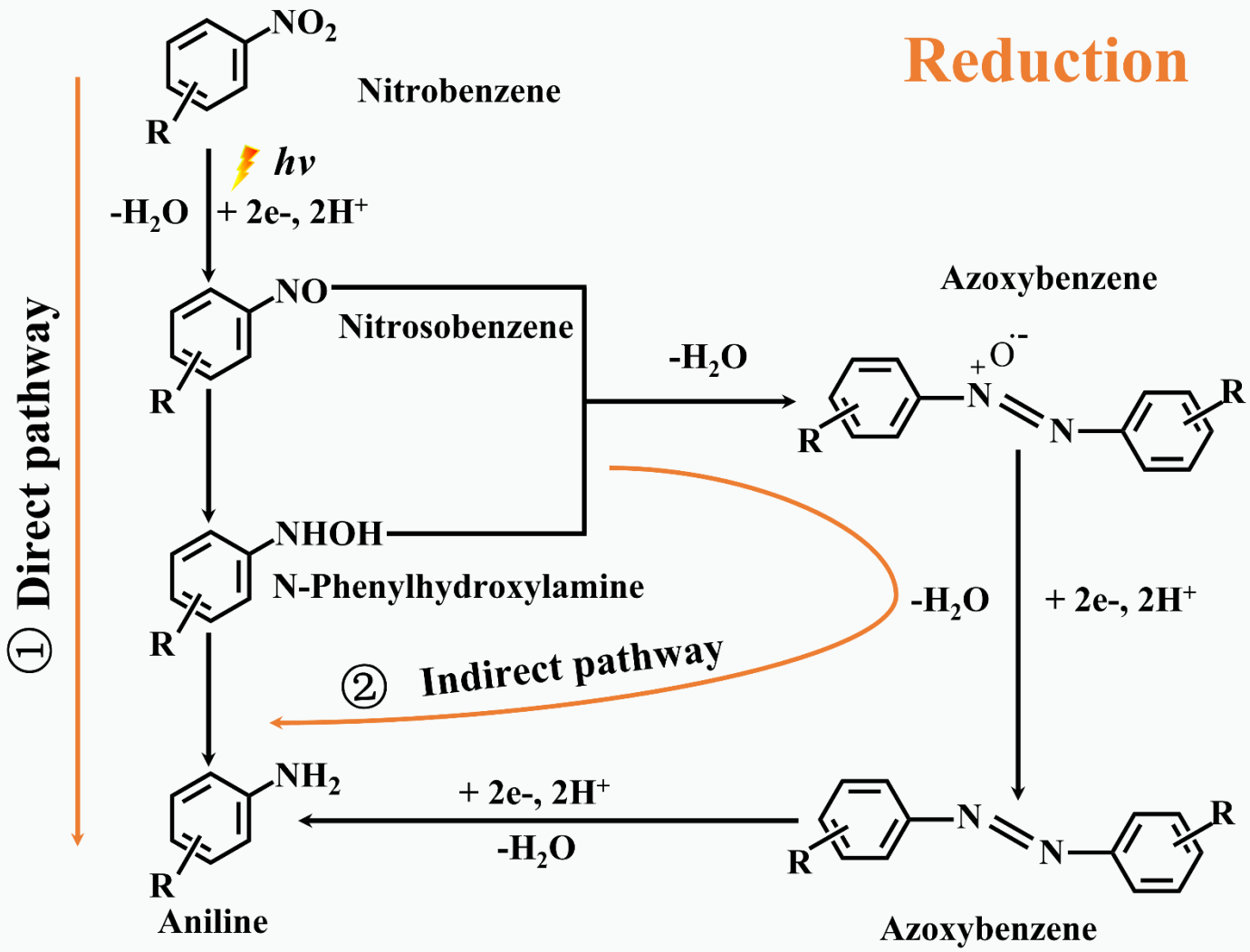

Figure S17. Photocatalytic mechanism of hydrogenation of nitroaromatics

Note: According to the previous works,[1, 2] there are two possible pathways for photocatalytic reduction of aromatic nitro compounds, which involve direct and indirect reaction pathways. The direct route involves gradual formation of nitrosobenzene (Ph-NO), phenylhydroxylamine (Ph-NHOH) and finally aniline (Ph-NH_2), following three consecutive hydrogenation steps. The second pathway, commonly named indirect or condensation route, involves the condensation of nitrosobenzene (Ph-N=NO-Ph), sequence azo (R-N=N-R), hydrazo (R-NH-NH-R), and finally aniline.

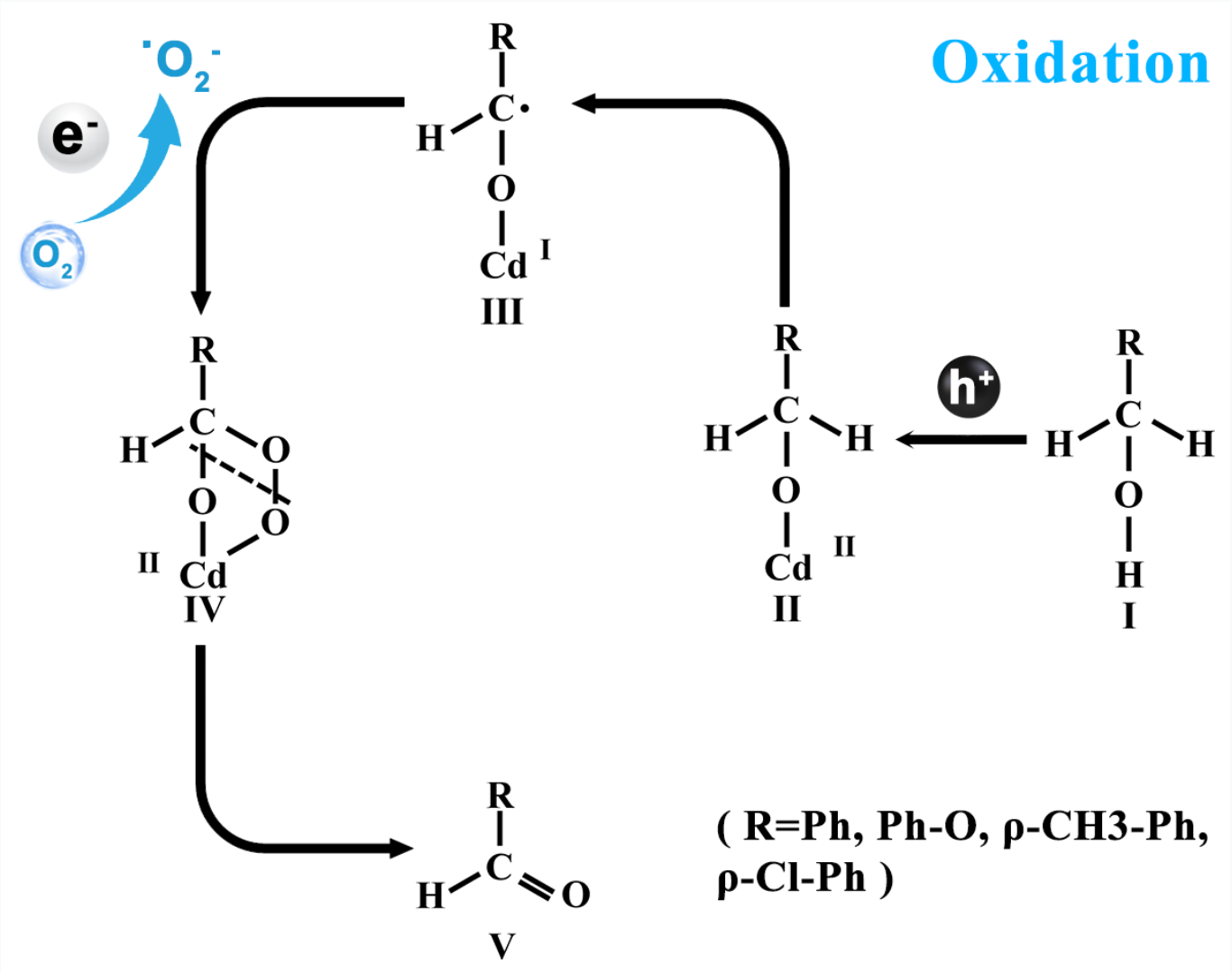

Figure S18. Photocatalytic mechanism of selective oxidation reaction

Note: Concerning the selective photocatalytic oxidation of aromatic alcohols to aldehydes, electrons injected into the CB of CdS are captured to generate Cd^{I} species and the alcohol molecules are adsorbed on the CdS surface to form structure **II** through deprotonation.[3-5] Subsequently, the adsorbent alcohol molecule first reacts with holes and then deprotonates to form carbon radicals, while electrons are captured by Cd^{I} to form Cd^{II}. It is worthwhile noting that electrons can directly combine with the dissolved O_2 molecules to engender superoxide ($^{\bullet}O_2^{-}$) radicals [$E°(O_2/^{\bullet}O_2^{-})$ = −0.284 V vs. NHE].[6] In this regard, the thus-formed $^{\bullet}O_2^{-}$ radicals take part in the oxidation of aromatic alcohols to aldehydes and attack the carbon radical to form intermediate **IV**, for which the interactions between the C–O bonds of the alcohol and O–O bonds of dioxygen may be synergistically realized through the oxygen-bridged structure **IV**.[7] Alternatively, holes accumulating in the HOMO level of alloyed NCs can also directly oxidize the aromatic alcohols to aldehydes, fulfilling the selective photocatalytic oxidation process.

Table S1. Peak position with corresponding functional groups for different samples.

Peak position (cm^{-1})	**$Au_{1-x}Ag_x$/CdS NWs**	**$Au_{1-x}Cu_x$/CdS NWs**	**$Au_{1-x}Pt_x$/CdS NWs**
3425	$-NH_2$, -OH [8, 9]	$-NH_2$, -OH	$-NH_2$, -OH
2920&2851	$-CH_2$ [10, 11]	$-CH_2$	$-CH_2$
1635	-COOH, $-NH_2$ [12]	-COOH, $-NH_2$	-COOH, $-NH_2$
1446	$-CH_3$ [9]	$-CH_3$	$-CH_3$
1039	-C-N- [8]	-C-N-	-C-N-

Table S2. Summary of the specific surface area, pore volume and pore size of CdS NWs and $Au_{1-x}Ag_x$/CdS NWs heterostructure.

Samples	S_{BET} $(m^2/g)^a$	*Total pore volume* $(cm^3/g)^b$	*Average pore size* $(nm)^c$
CdS NWs	22.2760	0.040400	7.2544
$Au_{1-x}Ag_x$ /CdS NWs	21.7130	0.036321	6.6911

[a] BET surface area is calculated from the linear part of BET plots.

[b] Single point total pore volume of the pores at P/P0 = 0.95.

[c] Adsorption average pore width (4V/A by BET).

Table S3. Chemical bond species vs. B.E. for different samples.

Elements	*CdS*	*$Au_{1-x}Ag_x$ NCs*	*Chemical Bond Species*
C 1s A	284.80	284.80	C-C
Cd $3d_{5/2}$	404.94	405.09	Cd^{2+} [13]
Cd $3d_{3/2}$	411.68	411.83	Cd^{2+}
S $2p_{3/2}$	161.43	161.51	S^{2-} [14]
S $2p_{1/2}$	162.64	162.70	S^{2-}
Au $4f_{5/2}$	/	87.85	Au^{0} [15, 16]
Au $4f_{5/2}$	/	88.45	Au^{+}
Au $4f_{7/2}$	/	84.28	Au^{0}
Au $4f_{7/2}$	/	84.77	Au^{+}
Ag $3d_{3/2}$	/	368.35	Ag^{+} [17, 18]
Ag $3d_{5/2}$	/	373.59	Ag^{+}

Table S4. ICP results of $Au_{1-x}Ag_x$ /CdS NWs heterostructure.

Element	*Concentration (wt.%)*	*RSD (%)*
Cd	76.5704	2.00
S	15.1494	4.78
Au	0.0085	5.10
Ag	0.0008	5.80

Table S5. Fitted EIS results of different samples based on the equivalent circuit.

Photoanodes	R_s / *ohm*	R_{ct} / *ohm*	*CPE* / ($\times 10^{-4}$ *F* cm^{-2})
CdS	15.77	7512	0.9874
$Au_{1-x}Ag_x$@GSH/CdS NWs	16.43	5935	0.7999

Note: As shown in Table S5, R_{ct} values were obtained by fitting the EIS results according to a simple equivalent circuit composed of a series of resistances **(Figure 5b, inset)**. Apparently, $Au_{1-x}Ag_x$/CdS NWs demonstrated the smallest R_{ct} value in comparison with other counterparts, indicative of its lowest interfacial charge transfer resistance.

Table S6. Time-resolved PL decay parameters of CdS NWs and $Au_{1-x}Ag_x$/CdS NWs.

Samples	τ_1 *(ns)*	τ_2 *(ns)*	A_1*(ns)*	A_2*(ns)*	τ_{aver} *(ns)*
CdS NWs	0.11	3.88	97.91	2.09	0.19
$Au_{1-x}Ag_x$ /CdS NWs	0.08	9.09	98.05	1.95	0.25

References

(1) Millán, R.; Liu, L.; Boronat, M.; Corma, A. A new molecular pathway allows the chemoselective reduction of nitroaromatics on non-noble metal catalysts. *J. Catal.* **2018**, *364*, 19-30.

(2) Yang, X. J.; Chen, B.; Zheng, L. Q.; Wu, L. Z.; Tung, C. H. Highly efficient and selective photocatalytic hydrogenation of functionalized nitrobenzenes. *Green Chem.* **2014**, *16* (3), 1082-1086.

(3) Benxia, L.; Ting, G.; Tian, M.; Junxin, W.; Peng, W.; Jianfang, W.; Yu, J. C. (Gold Core)@(Ceria Shell) Nanostructures for Plasmon-Enhanced Catalytic Reactions under Visible Light. *ACS Nano* **2014**, *8*, 8152-8162.

(4) Abad, A.; Concepción, P.; Corma, A.; García, H. A Collaborative Effect between Gold and a Support Induces the Selective Oxidation of Alcohols. *Angew. Chem., Int. Ed.* **2005**, *44* (26), 4066-4069.

(5) Zhang, M.; Chen, C.; Ma, W.; Zhao, J. Visible-Light-Induced Aerobic Oxidation of Alcohols in a Coupled Photocatalytic System of Dye-Sensitized TiO_2 and TEMPO. *Angew. Chem., Int. Ed.* **2008**, *47* (50), 9730-9733.

(6) Zhang, L. J.; Li, S.; Liu, B. K.; Wang, D. J.; Xie, T. F. Highly Efficient CdS/WO_3 Photocatalysts: Z-Scheme Photocatalytic Mechanism for Their Enhanced Photocatalytic H_2 Evolution under Visible Light. *ACS Catal.* **2014**, *4* (10), 3724-3729.

(7) Wallar, B. J.; Lipscomb, J. D. Dioxygen Activation by Enzymes Containing Binuclear Non-Heme Iron Clusters. *Chem. Rev* **1996**, *96*, 2625-2658.

(8) Fu, X. Y.; Li, Y. B.; Huang, M. H.; Li, T.; Dai, X. C.; Hou, S.; Wei, Z. Q.; Xiao, F. X. Partially Self-Transformed Transition-Metal Chalcogenide Interim Layer: Motivating Charge Transport Cascade for Solar Hydrogen Evolution. *Inorg. Chem.* **2020**, *59* (4), 2562-2574.

(9) Huang, M. H.; Li, Y. B.; Li, T.; Dai, X. C.; Hou, S.; He, Y.; Xiao, G.; Xiao, F. X. Self-transformation of ultra-small gold nanoclusters to gold nanocrystals toward boosted photoreduction catalysis. *Chem. Commun.* **2019**, *55* (71), 10591-10594.

(10) Wei, Z. Q.; Hou, S.; Lin, X.; Xu, S.; Dai, X. C.; Li, Y. H.; Li, J. Y.; Xiao, F. X.; Xu, Y. J. Unexpected Boosted Solar Water Oxidation by Nonconjugated Polymer-Mediated Tandem Charge Transfer. *J. Am. Chem. Soc.* **2020**, *142* (52), 21899-21912.

(11) Xiao, F. X.; Hung, S. F.; Miao, J.; Wang, H. Y.; Yang, H.; Liu, B. Metal-Cluster-Decorated TiO_2 Nanotube Arrays: A Composite Heterostructure toward Versatile Photocatalytic and Photoelectrochemical Applications. *Small* **2014**, *11* (5), 554-567.

(12) Xiao, F. X.; Liu, B. In situ etching-induced self-assembly of metal cluster decorated one-dimensional semiconductors for solar-powered water splitting: unraveling cooperative synergy by photoelectrochemical investigations. *Nanoscale* **2017**, *9* (43), 17118-17132.

(13) Nikam, P. R.; Baviskar, P. K.; Sali, J. V.; Gurav, K. V.; Kim, J. H.; Sankapal, B. R. CdS surface encapsulated ZnO nanorods: Synthesis to solar cell application. *J. Alloys Compd.* **2016**, *689*, 394-400.

(14) Yan, Z.; Yu, X.; Han, A.; Xu, P.; Du, P. Noble-Metal-Free Ni$(OH)_2$-Modified CdS/Reduced Graphene Oxide Nanocomposite with Enhanced Photocatalytic Activity for Hydrogen Production under Visible Light Irradiation. *J. Phys. Chem. C* **2014**, *118* (40), 22896-22903.

(15) Li, Z. Y.; Chen, Y. H.; Zhu, J. R.; Chen, Q.; Lu, S. J.; Xiao, F. X. Self-Transformation of Atomically Precise Alloy Nanoclusters to Plasmonic Alloy Nanocrystals: Evaluating Photosensitization in Solar Water Oxidation. *Inorg. Chem.* **2023**, *62* (41), 16965-16973.

(16) Su, P.; Tang, B.; Xiao, F. X. Layer-By-Layer Assembly of Atomically Precise Alloy Nanoclusters Photosystems for Solar Water Oxidation. *Small* **2023**, *20* (7).

(17) Pal, N. K.; Kryschi, C. A facile UV-light mediated synthesis of l-histidine stabilized silver nanocluster for efficient photodegradation of methylene blue. *J. Mol. Catal. A: Chem.* **2015**, *404-405*, 27-35.

(18) Zheng, K. y.; Yuan, X.; Kuah, K.; Luo, Z. T.; Yao, Q. F.; Zhang, Q. B.; Xie, J. P. Boiling water synthesis

of ultrastable thiolated silver nanoclusters with aggregation-induced emission. *Chem. Commun.* **2015**, *51* (82), 15165-15168.